INTERFACE

royalsocietypublishing.org/journal/rsif

Research

Cite this article: Jin W, Alastruey J. 2021 Arterial pulse wave propagation across stenoses and aneurysms: assessment of one-dimensional simulations against three-dimensional simulations and *in vitro* measurements. *J. R. Soc. Interface* **18**: 20200881.
https://doi.org/10.1098/rsif.2020.0881

Received: 31 October 2020
Accepted: 17 March 2021

Subject Category:
Life Sciences–Engineering interface

Subject Areas:
bioengineering, biomedical engineering

Keywords:
haemodynamics, mathematical modelling, pulse wave propagation, computational fluid dynamics, *in vitro* measurements

Author for correspondence:
Jordi Alastruey
e-mail: jordi.alastruey-arimon@kcl.ac.uk

Electronic supplementary material is available online at https://doi.org/10.6084/m9.figshare.c.5361994.

THE ROYAL SOCIETY PUBLISHING

Arterial pulse wave propagation across stenoses and aneurysms: assessment of one-dimensional simulations against three-dimensional simulations and *in vitro* measurements

Weiwei Jin[1] and Jordi Alastruey[1,2]

[1]Department of Biomedical Engineering, King's College London, London, UK
[2]World-Class Research Center 'Digital Biodesign and Personalized Healthcare', Sechenov University, Moscow, Russia

WJ, 0000-0002-0919-2470; JA, 0000-0003-3742-5259

One-dimensional (1-D) arterial blood flow modelling was tested in a series of idealized vascular geometries representing the abdominal aorta, common carotid and iliac arteries with different sizes of stenoses and/or aneurysms. Three-dimensional (3-D) modelling and *in vitro* measurements were used as ground truth to assess the accuracy of 1-D model pressure and flow waves. The 1-D and 3-D formulations shared identical boundary conditions and had equivalent vascular geometries and material properties. The parameters of an experimental set-up of the abdominal aorta for different aneurysm sizes were matched in corresponding 1-D models. Results show the ability of 1-D modelling to capture the main features of pressure and flow waves, pressure drop across the stenoses and energy dissipation across aneurysms observed in the 3-D and experimental models. Under physiological Reynolds numbers (Re), root mean square errors were smaller than 5.4% for pressure and 7.3% for the flow, for stenosis and aneurysm sizes of up to 85% and 400%, respectively. Relative errors increased with the increasing stenosis and aneurysm size, aneurysm length and Re, and decreasing stenosis length. All data generated in this study are freely available and provide a valuable resource for future research.

1. Introduction

Computational blood flow modelling can provide valuable insights into the assessment of cardiovascular disease. The most common formulations for vascular blood flow modelling are zero-dimensional (0-D), one-dimensional (1-D) and three-dimensional (3-D) models. Lumped parameter (or 0-D) models provide compartmental representations of the cardiovascular system. They have been used to study whole-body haemodynamics, including cardiac dynamics [1], and time-variant haemodynamics involving activities such as postural change [2] and exercise [3,4]. A 0-D approach is computationally inexpensive (analytical solutions are often possible), but is not suitable for describing pulse wave propagation and complex flow phenomena occurring in blood vessels. On the other hand, 3-D modelling based on the incompressible Navier–Stokes equations can describe pulse wave propagation [5] and complex flow phenomena; for example, 3-D flow patterns and mechanical stresses resulting from interactions between blood flow and the vessel wall in stenoses [6,7] and aneurysms [8,9]. However, this comes at a considerably higher computational cost than the 0-D and 1-D modelling approaches [10,11]. 3-D simulations require of the order of hours (even days) to compute the solution using high-performance computers, whereas 0-D and 1-D models take of the order of seconds or minutes on standard PCs.

Table 1. Literature review of studies on 1-D modelling accuracy. The third column shows the type of reference data used in each study. Upper bounds for relative errors for pressure (ε_P), flow rate (ε_Q), flow velocity (ε_U) and cross-sectional area (ε_A) wave morphology, calculated as described in the corresponding article, are shown when available.

reference		test data	simulated arteries	ε_P	ε_Q	ε_U	ε_A
Matthys *et al.*	[12]	*in vitro*	37 larger arteries	4.0%	19.0%	—	—
Bessems *et al.*	[22]	*in vitro*	Ao[a]	*	*	—	—
Alastruey *et al.*	[13]	*in vitro*	37 larger arteries	2.5%	10.8%	—	—
Saito *et al.*	[14]	*in vitro*	9 larger arteries	10.0%	*	—	—
Huberts *et al.*	[23]	*in vitro*	upper-limb arteries	*	*	—	—
Boileau *et al.*	[15]	*in vitro*	37 larger arteries	4.0%	25.6%	—	—
Avolio	[24]	human	128 larger arteries	—	—	*	—
Stettler *et al.*	[25,26]	human	Ao and lower-limb arteries	*	*	—	—
Olufsen *et al.*	[27]	human	29 larger arteries	—	*	—	—
Reymond *et al.*	[16]	human	103 larger arteries	*	*	—	—
Reymond *et al.*	[17]	human	94 larger arteries	6.0%[b]	11.0%	—	—
Willemet *et al.*	[18]	human	lower-limb arteries	9.6%	—	16.0%	—
Alastruey *et al.*	[19]	human	upper Ao and supra Ao arteries	10.0%	7.0%	—	8.0%
Strocchi *et al.*	[28]	human	55 larger arteries	*	*	—	—
Steele *et al.*	[20]	animal	aortic bypass	—	4.2%		
Mynard *et al.*	[21]	animal	left conduit coronary arteries	—	16.7%	—	—
Mynard *et al.*	[29]	3-D data	carotid bifurcation	—	—	*	—
Grinberg *et al.*	[30]	3-D data	50 larger intracranial arteries	*	*	—	—
Xiao *et al.*	[11]	3-D data	CCA, thoracic Ao, aortic bifurcation	1.4%	2.1%	—	2.6%
Xiao *et al.*	[11]	3-D data	20 larger arteries	2.1%	4.9%	—	—
Boileau *et al.*	[15]	3-D data	CCA, thoracic Ao, aortic bifurcation	1.2%	2.6%	—	4.3%
Alastruey *et al.*	[19]	3-D data	upper Ao and supra Ao arteries	2.0%	5.0%	—	3.0%

Ao, aorta; CCA, common carotid artery.
*Qualitative comparison only.
— No comparison made.
[a]According to the dimensions shown in fig. 4 of [22].
[b]Except at the abdominal aorta, where root mean square error is 21%.

Several studies have shown that 1-D models—in which the 3-D space dependency is reduced to the vessel's axial coordinate only—are a good compromise between accuracy and computational cost to simulate pulse wave propagation in large arterial networks. This has been achieved through various comparisons of 1-D model pressure, flow and cross-sectional area waves against *in vitro* data acquired in experimental set-ups of the aorta and its larger branches made of flexible tubes [12–15], *in vivo* data acquired in humans [16–19] and animals [20,21], and numerical data obtained by solving the full 3-D equations of blood flow in compliant vessels [11,15,19]. These studies have mainly focused on assessing the accuracy of 1-D modelling under normal anatomical conditions, which are characterized by the presence of tapering, junctions and vessel curvature and torsion. They reported relative root mean square errors (RMSEs) between 1-D model and reference waveforms of as little as 1.2% for pressure, 2.1% for the flow and 2.6% for the cross-sectional area (table 1).

The effect on 1-D modelling accuracy of localized changes in vascular geometry—for example those occurring in diseased vasculatures with stenoses and aneurysms—has received less attention. Sterogiopulos *et al.* investigated the effects of arterial stenoses on arterial pulse waveforms, though the accuracy of the 1-D formulation used in their studies was evaluated by qualitative comparisons with previous computational and *in vivo* studies [31] and quantitative comparisons of stenosis reflection coefficients against *in vitro* data [32], without assessing 1-D model pressure and flow waveforms. Wan *et al.* [33] computed 1-D and 3-D model haemodynamics on a patient-specific arterial network of the abdominal aorta and larger lower-limb arteries with several localized changes in luminal cross-sectional area due to the presence of occlusive disease. However, they focused their study on assessing mean flow rates rather than pulse waveforms. In all those studies, pressure losses across stenoses were described in the 1-D formulation based on empirical data [34,35]. Papadakis & Raspaud [36] compared 1-D model pressure and flow velocity data obtained both analytically and computationally in an idealized stenotic carotid artery (with a 75% stenosis size) against corresponding data obtained using a 3-D model. They showed a very good agreement between 1-D and 3-D model flow waveforms, with relative errors smaller than 1.0%, though the 1-D model pressure wave was severely underpredicted at the inlet.

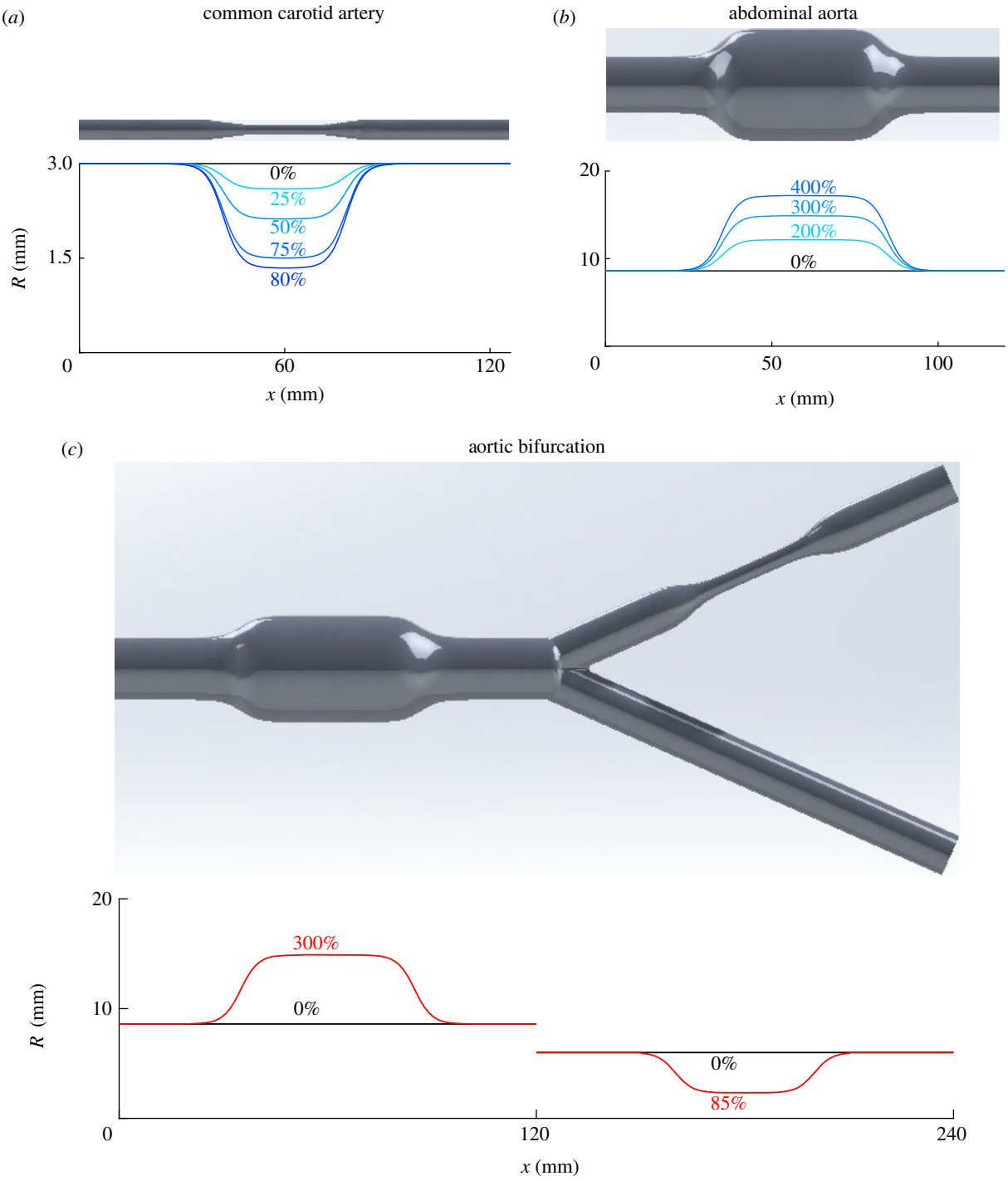

Figure 1. The idealized vascular geometries studied: common carotid artery with a stenosis (*a*), abdominal aorta with an aneurysm (*b*) and aortic bifurcation with an aneurysm in the abdominal aorta and a stenosis in the left iliac artery (*c*). Their luminal radius variations are shown in the corresponding plots, at baseline (black lines) and for different percentage degrees of stenosis and aneurysm (coloured lines).

A small number of studies have simulated blood flow across aneurysms using 1-D modelling [37–39]. These include comparisons against experimental measurements in idealized [38] and anatomically correct [39] geometries; yet the accuracy of 1-D model pulse waveforms was not quantified.

Geometrical multiscale models in which the 3-D, 1-D and 0-D formulations are mathematically coupled to form a unique model [40–42] have also been used to simulate blood flow in vessels with aneurysms and/or stenoses [43–46]. This alternative numerical approach reduces the computational cost of full 3-D models, though 3-D/1-D/0-D multiscale modelling is still computationally more expensive than 1-D modelling (coupled to 0-D outflow boundary conditions), which is the focus of this study.

This study aims to assess the ability of the 1-D formulation to simulate pulse wave propagation in arteries with localized changes in cross-sectional area due to the presence of a stenosis and/or aneurysm. 1-D model pressure and flow waveforms were compared against corresponding waveforms simulated by a 3-D formulation of blood flow in compliant vessels with identical boundary conditions and equivalent vascular geometries and material properties. We considered three idealized vascular geometries representing a human (i) common carotid artery (CCA) with a stenosis (figure 1*a*), (ii) abdominal aorta with an aneurysm (i.e. an AAA) (figure 1*b*), and (iii) aortic bifurcation with an AAA and a stenosis in the left iliac artery (figure 1*c*). Furthermore, 1-D model pressure waveforms in the abdominal aorta with

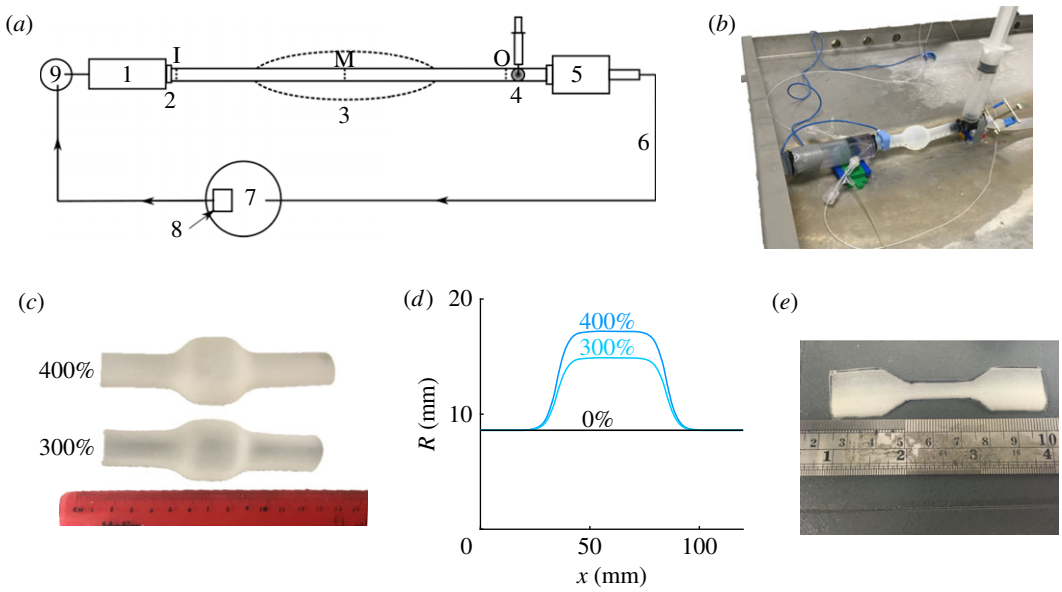

Figure 2. *In vitro* experimental set-up. (*a*) Schematic showing the piston-driven ventricle (1); aortic valve (2); aneurysm site (3); Windkessel model (4); peripheral drain box (5); guttering system (6); reservoir (7); submersible pump (8); and atrium (9). (*b*) Photo of the aortic part of the experimental set-up. (*c*) 300% and 400% aneurysm phantoms made of Agilus 30 clear resin. (*d*) Luminal radius variations. (*e*) Specimen for material property testing. The three perpendicular dash lines (I, inlet; M, middle; O, outlet) along the phantom in (*a*) indicate the sites where 1-D model pressures were compared with *in vitro* measurements.

an AAA were compared against *in vitro* measurements acquired in a 1 : 1 scale cardiovascular simulator rig of the human aorta (figure 2).

2. Methods

2.1. 1-D and 3-D simulations

2.1.1. Generating vascular geometries

All 3-D vascular geometries used in this study were created using SolidWorks (Dassault Systémes SolidWorks Corporation, Vélizy-Villacoublay, France). They were obtained by rotating the radius variations shown in figure 1 about the centreline of the corresponding vessels. Vascular dimensions were based on the values provided by Xiao *et al.* [11]. A range of stenosis lengths and sizes representative of real human stenoses [47] were simulated in the middle of the CCA using the luminal radius variations shown in figure 1*a*. The size of the stenosis was defined as $(1 - A_S/A_0) \times 100\%$, with A_S the minimum luminal cross-sectional area within the stenosis and A_0 the area proximal to the stenosis. A range of aneurysm lengths and sizes representative of real human aneurysms [48,49] were simulated in the middle of the abdominal aorta using the luminal radius variations shown in figure 1*b*. The size of the aneurysm was defined as $A_A/A_0 \times 100\%$, with A_A the maximum luminal cross-sectional area within the aneurysm and A_0 the area proximal to the aneurysm.

For each geometry, 3-D tetrahedral meshes were generated using MeshSim (Simmetrix Inc., NY, USA), with an absolute mesh size of 0.3 mm for the CCA and 0.45 mm for the abdominal aorta and aortic bifurcation. Boundary layer meshing of three layers was applied to all cases, with a total thickness of 0.5 mm for the CCA and 1 mm for the abdominal aorta and aortic bifurcation. The total number of elements in each case varied depending on the size of the stenosis or aneurysm; from 985 826 to 1 490 212 for the CCA, from 2 514 454 to 5 959 180 for the abdominal aorta and from 5 016 316 to 7 029 817 for the aortic bifurcation. The characteristics of the meshes used for the baseline geometries (i.e. without a stenosis or aneurysm) are based on the equivalent geometries in [11], for which mesh independence studies were undertaken. Compatible 1-D geometries with the same radius variation as the 3-D geometries were generated using Matlab (The MathWorks, Natick, MA, USA). Finite-element meshes with a size of up to 1.2 cm were used for all simulations.

2.1.2. 1-D and 3-D haemodynamic models

The 1-D formulation was solved using our in-house solver Nektar1D [50]; 3-D simulations were performed using the open-source software CRIMSON [51]. Corresponding 1-D and 3-D simulations shared compatible geometries and material properties and had identical inflow/outflow boundary conditions. Fully developed Poiseuille flows (figure 3*a*) were prescribed at the inlets and three-element Windkessel models (figure 3*b* and table 2) were coupled at the outlets. An empirically based model [33] was used to calculate pressure losses across the stenosis in the 1-D simulations, hereafter referred to as the 'stenosis model'. All 1-D simulations were run on a standard PC (MacBook Pro; 2.7 GHz Quad-Core Intel Core i7), whereas all 3-D model simulations were run on a high-performance computer (SGI Altix UV 1000). All 1-D and 3-D simulations were run for multiple cardiac cycles until a periodic solution was achieved in which the values of diastolic blood pressure at the start and end of the last cycle differed by less than 0.5%. The haemodynamic properties of the three models in figure 1 were taken from the properties of the corresponding models in Xiao *et al.* [11]. All models in this study considered blood to be an incompressible Newtonian fluid and blood flow to be laminar.

2.1.3. 1-D formulation

The governing equations of the 1-D model were [50]

$$\frac{\partial A}{\partial t} + \frac{\partial (AU)}{\partial x} = 0, \tag{2.1}$$

$$\frac{\partial U}{\partial t} + U\frac{\partial U}{\partial x} + \frac{1}{\rho}\frac{\partial P}{\partial x} = \frac{f}{\rho A} \tag{2.2}$$

and

$$P = P_d + \frac{\beta}{A_d}\left(\sqrt{A} - \sqrt{A_d}\right), \tag{2.3}$$

where $A(x, t)$ is the luminal cross-sectional area, $U(x, t)$ is the blood flow velocity, $P(x, t)$ is the arterial blood pressure, t is time and x is the axial coordinate. The density of blood, ρ, was taken to be 1060 kg m^{-3} to match the value used in the 3-D simulations. The frictional term per unit length, $f(x, t) = \eta U$, was assumed to be proportional to U, with the viscous loss function,

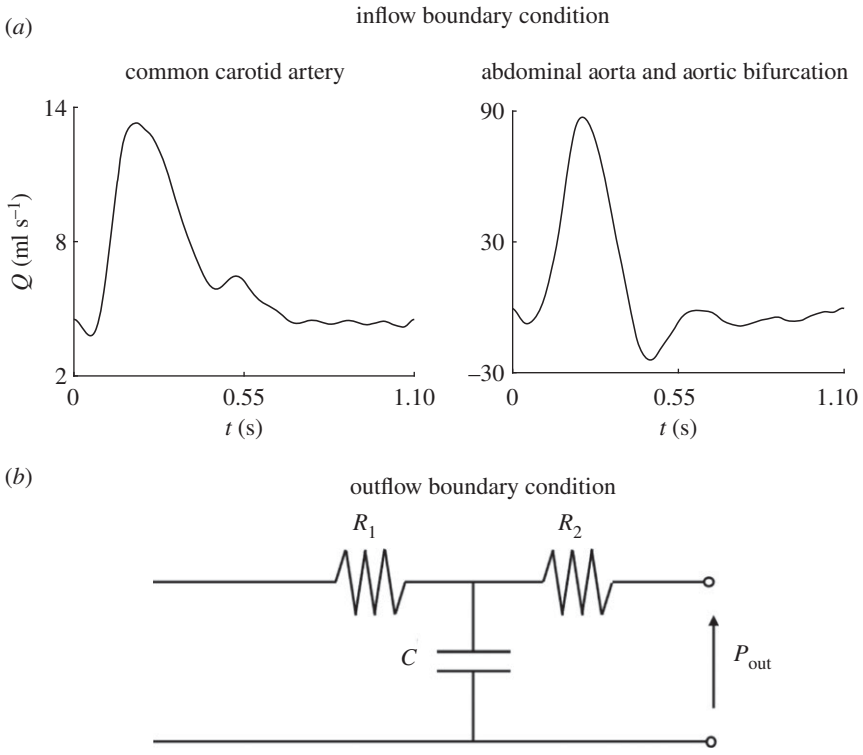

Figure 3. Inflow (*a*) and outflow (*b*) boundary conditions used in this study. The parameters of the outflow boundary conditions are shown in table 2.

Table 2. Parameters of the outflow three-element Windkessel models (figure 3*b*) used in this study. Outflow blood pressures P_{out} were assumed to be zero in all cases.

	common carotid artery	abdominal aorta	aortic bifurcation
R_1 (mmHg s ml^{-1})	1.8658	0.0881	0.5110
C (ml mmHg^{-1})	0.0234	1.3550	0.0489
R_2 (mmHg s ml^{-1})	14.0239	0.8376	23.2617

η, described in the next section. In the tube law (equation (2.3)), the subscript d denotes the diastolic value and β accounts for the stiffness of the arterial wall,

$$\beta = \frac{3}{4}\sqrt{\pi}Eh, \tag{2.4}$$

where E is Young's modulus and h is the wall thickness. The time step for all 1-D simulations was 10^{-5} s.

2.1.4. Stenosis model

An empirically based stenosis model [35] was introduced into the 1-D formulation through the frictional term $f = \eta U$ in equation (2.2), based on a previous study [33]. The viscous loss function, η, was the theoretical expression

$$\eta_0 = -2(\zeta + 2)\mu\pi \tag{2.5}$$

outside the stenosis and the empirical expression

$$\eta_S = \eta_0 + \frac{-A_S^2 Q_0^2 \left[\frac{K_v}{Re_0} + \frac{K_t}{2}\left(\frac{A_0}{A_S} - 1\right)^2\right]}{A_0^2 Q_S L_S} \tag{2.6}$$

within the stenosis. The subscript '0' refers to the arterial region proximal and distal to the stenosis, whereas the subscript 'S' refers to the arterial region within the stenosis. Blood viscosity, $\mu = 4$ mPa s, matches the value used in 3-D simulations, $Q = AU$ is the blood flow, $Re_0 = \rho U_0 D_0/\mu$ is the Reynolds number, with U_0 the flow velocity at a given time and D_0 the cross-sectional diameter, L_S is the length of the stenosis, $K_t = 1.52$ and

$$K_v = 32\frac{L_S}{D_0}\left(\frac{A_0}{A_S}\right)^2. \tag{2.7}$$

2.1.5. 3-D formulation

CRIMSON enabled us to solve a 3-D fluid–structure interaction (FSI) problem in which blood flow was governed by the 3-D Navier–Stokes equations for an incompressible Newtonian fluid. The FSI problem was solved by using the 'enhanced' membrane formulation proposed by Figueroa *et al.* [51], in which vessel wall displacements are described as a function of blood velocity and pressure at the interface. In addition, external tissue support was used in all simulations to account for the tethering exertion and to eliminate spurious and non-physiological oscillations [52]. A detailed description of the 3-D formulation can be found in [51]. The time step for all 3-D simulations was 2×10^{-4} s.

2.2. *In vitro* experimental set-up

The experimental cardiovascular simulator rig developed by Gaddum *et al.* [53] (figure 2*a*,*b*) was used to produce additional pulse wave data for the abdominal aorta case study with a 0%, a 300% and a 400% aneurysm (figure 2*c*,*d*). All AAA phantoms were made of Agilus 30 clear resin (Deed3d Technology Co., Ltd, Guangzhou, China) (samples shown in figure 2*c*). These flexible phantoms were fixed on the connectors after the aortic valve (figure 2*a*,(2)) and before the Windkessel model (figure 2*a*,(4)) in the experimental system using cable ties. Although some studies [54] have used blood-mimicking fluids, here water was used. As shown in figure 2*b*, an ultrasound-based flow sensor (COnfidence Flowprobes for Research (PAU Series); Transonic, Ithaca, NY, USA) and a pressure catheter (Mikro-Cath™ 3.5F; Millar, Houston, TX, USA) were fixed at the inlet of the

abdominal aorta phantom to measure the flow and pressure waves. A second pressure catheter was used to measure the pressure wave at the inlet, middle and outlet of the aortic phantom. All flow and pressure sensors were calibrated at the start of each phantom measurement. The sampling rate of pressure and flow measurements was 1000 kHz. On average, 30 cardiac cycles were acquired at each measurement point. Samples from the phantom (figure 2*e*) were taken to estimate Young's modulus using a uniaxial extension test. The test was performed using an electromechanical test system (5500 series; Instron, Wycombe, UK) on five different specimens taken from the AAA phantoms.

The data analysis was performed offline in Matlab. The signals were first filtered with a low-pass filter to reduce noise while maintaining the relevant frequency information. Subsequently, 15 beats were selected from the recorded beats and ensemble-averaged to generate a single beat pressure and flow waveform (with an ensemble standard deviation) to be compared with their numerical counterparts. The ensemble-averaged flow waves measured at the inlet of the aortic phantom were taken as the inflow boundary conditions for the 1-D simulations. The ensemble-averaged pressure measured by the first sensor fixed at the inlet of the aortic phantom was taken as a reference to calibrate the pressure measured by the second sensor at different positions along the phantom. Finally, the 1-D model parameters of the three-element Windkessel outflow boundary condition were calculated using the inflow boundary condition and the pressure waveform at the inlet using the algorithm described in [55].

2.3. Error calculations

The following relative error metrics were used to quantify the accuracy of the pressure, P, and flow, Q, waveforms computed by the 1-D formulation:

$$\left.\begin{aligned} \epsilon_P^{\mathrm{RMS}} &= \sqrt{\frac{1}{n}\sum_{i=1}^{n}\left(\frac{P_i^{\mathrm{1D}}-P_i^{\mathrm{Ref}}}{P_i^{\mathrm{Ref}}}\right)}, & \epsilon_Q^{\mathrm{RMS}} &= \sqrt{\frac{1}{n}\sum_{i=1}^{n}\left(\frac{Q_i^{\mathrm{1D}}-Q_i^{\mathrm{Ref}}}{\max(Q^{\mathrm{Ref}})}\right)},\\ \epsilon_P^{\mathrm{MAX}} &= \max_i\left|\frac{P_i^{\mathrm{1D}}-P_i^{\mathrm{Ref}}}{P_i^{\mathrm{Ref}}}\right|, & \epsilon_Q^{\mathrm{MAX}} &= \max_i\left|\frac{Q_i^{\mathrm{1D}}-Q_i^{\mathrm{Ref}}}{\max(Q^{\mathrm{Ref}})}\right|,\\ \epsilon_P^{\mathrm{SYS}} &= \frac{\max(P^{\mathrm{1D}})-\max(P^{\mathrm{Ref}})}{\max(P^{\mathrm{Ref}})}, & \epsilon_Q^{\mathrm{SYS}} &= \frac{\max(Q^{\mathrm{1D}})-\max(Q^{\mathrm{Ref}})}{\max(Q^{\mathrm{Ref}})},\\ \epsilon_P^{\mathrm{DIAS}} &= \frac{\min(P^{\mathrm{1D}})-\min(P^{\mathrm{Ref}})}{\min(P^{\mathrm{Ref}})}, & \epsilon_Q^{\mathrm{DIAS}} &= \frac{\min(Q^{\mathrm{1D}})-\min(Q^{\mathrm{Ref}})}{\max(Q^{\mathrm{Ref}})}, \end{aligned}\right\} \tag{2.8}$$

where n is the number of points in one cardiac cycle, P_i^{1D} and Q_i^{1D} are, respectively, the pressure and flow results obtained at each time point $i = 1,\ldots,n$ from the 1-D simulation at a single spatial location, and P_i^{Ref} and Q_i^{Ref} are the corresponding reference results obtained from the 3-D model or, for P_i^{Ref} only, the *in vitro* experimental set-up. 3-D model reference values were calculated as the cross-sectional averaged pressure and flow at each point $i = 1,\ldots,n$ at a single cross-section perpendicular to the vessel centreline. $\epsilon_P^{\mathrm{RMS}}$ and $\epsilon_Q^{\mathrm{RMS}}$ are the root mean square relative errors for pressure and flow; $\epsilon_P^{\mathrm{MAX}}$ and $\epsilon_Q^{\mathrm{MAX}}$ are the maximum relative errors for pressure and flow; $\epsilon_P^{\mathrm{SYS}}$ and $\epsilon_Q^{\mathrm{SYS}}$ are the relative errors in systolic pressure and flow; $\epsilon_P^{\mathrm{DIAS}}$ and $\epsilon_Q^{\mathrm{DIAS}}$ are the relative errors in diastolic pressure and flow. $\max(Q^{\mathrm{Ref}})$ is the maximum value of the reference flow rate.

A relative error metric, $\epsilon_{\delta P}$, was used to quantify the accuracy of the pressure drop (δP) estimated by the 1-D formulation (superscript '1D') relative to the value obtained from the corresponding 3-D simulations (superscript '3D'),

$$\epsilon_{\delta P} = \frac{|\delta P^{\mathrm{1D}} - \delta P^{\mathrm{3D}}|}{\bar{P}^{\mathrm{3D}}_{\mathrm{prox}}}. \tag{2.9}$$

δP was calculated as the difference in the mean blood pressure ($\bar{P}$) measured at 5 mm proximal and 5 mm distal to the stenosis. Notably, the denominator, $\bar{P}^{\mathrm{3D}}_{\mathrm{prox}}$, is the mean blood pressure measured 5 mm proximal to the stenosis in the 3-D model.

In addition, the inaccuracies introduced by the inability of the 1-D formulation to simulate the intricate 3-D flow patterns within the aneurysm were assessed by comparing the energy dissipation between the 1-D and 3-D simulations. The energy dissipation, E_{diss}, was calculated as the change in energy flux between the proximal (subscript 'prox') and distal (subscript 'dist') sites of the aneurysm [56],

$$\left.\begin{aligned} E_{\mathrm{diss}} &= E_{\mathrm{prox}} - E_{\mathrm{dist}},\\ E_{\mathrm{prox}} &= Q_{\mathrm{prox}}\left(P_{\mathrm{prox}} + \tfrac{1}{2}\rho U^2_{\mathrm{prox}}\right)\\ \text{and}\quad E_{\mathrm{dist}} &= Q_{\mathrm{dist}}\left(P_{\mathrm{dist}} + \tfrac{1}{2}\rho U^2_{\mathrm{dist}}\right), \end{aligned}\right\} \tag{2.10}$$

where E_{prox} and E_{dist} are the energy flux at 5 mm proximal and 5 mm distal to the aneurysm, respectively. The following relative error metric ($\epsilon_{E_{\mathrm{diss}}}$) was used to quantify the accuracy of the energy dissipation estimated by the 1-D simulation (superscript '1D') relative to the value obtained from the 3-D simulation (superscript '3D'):

$$\epsilon_{E_{\mathrm{diss}}} = \frac{|E^{\mathrm{1D}}_{\mathrm{diss}} - E^{\mathrm{3D}}_{\mathrm{diss}}|}{E^{\mathrm{3D}}_{\mathrm{prox}}}. \tag{2.11}$$

Notably, the denominator, $E^{\mathrm{3D}}_{\mathrm{prox}}$, is the energy flux at 5 mm proximal to the aneurysm in the 3-D model.

3. Results

3.1. Assessment against 3-D model data

All idealized geometries representing typical CCA, AAA and aortic bifurcation with AAA and iliac stenosis shown in figure 1 were used for the systematic comparison of 1-D and 3-D modelling schemes. Each 1-D model simulation took less than 2 min for the CCA (18 cardiac cycles were run), 5 min for the abdominal aorta (30 cycles) and 9 min for the aortic bifurcation (30 cycles) on a standard PC, whereas corresponding 3-D model simulations required over 1 day for the CCA (10 cycles), 4 days for the abdominal aorta (12 cycles) and 7 days for the aortic bifurcation (16 cycles) using 64 processors on a high-performance computer. All relative errors for 1-D model waveforms obtained at baseline (i.e. without a stenosis or aneurysm) in the CCA, abdominal aorta and aortic bifurcation are consistent with the relative errors reported by Xiao *et al.* [11] in the same vascular geometries. These include root mean square relative errors (ϵ^{RMS}) smaller than 1% for pressure and 2% for the flow for all cases. Electronic supplementary material, figures S1 (top), S6 (top) and S9 show comparisons of 1-D model pressure and flow waves against corresponding 3-D model waves in the CCA, abdominal aorta and aortic bifurcation, respectively, at baseline.

3.1.1. CCA with a stenosis

Figure 4*b* compares 1-D model pressure and flow waveforms at 5 mm proximal, the middle and 5 mm distal to a 75%, 48-mm-long stenosis with corresponding 3-D model results. At those measurement sites, ϵ_{RMS} remained smaller than 1.5% for both pressure and flow waves when a stenosis of up to 75% in size was present in the middle of the vessel, for a physiological Reynolds number (Re) of 345. (All Re values reported in the Results section were calculated at peak flow velocity.) 1-D model pressure and flow waves were able to reproduce the main features of corresponding 3-D model waves, including the ripples observed for the pressure and flow waves in

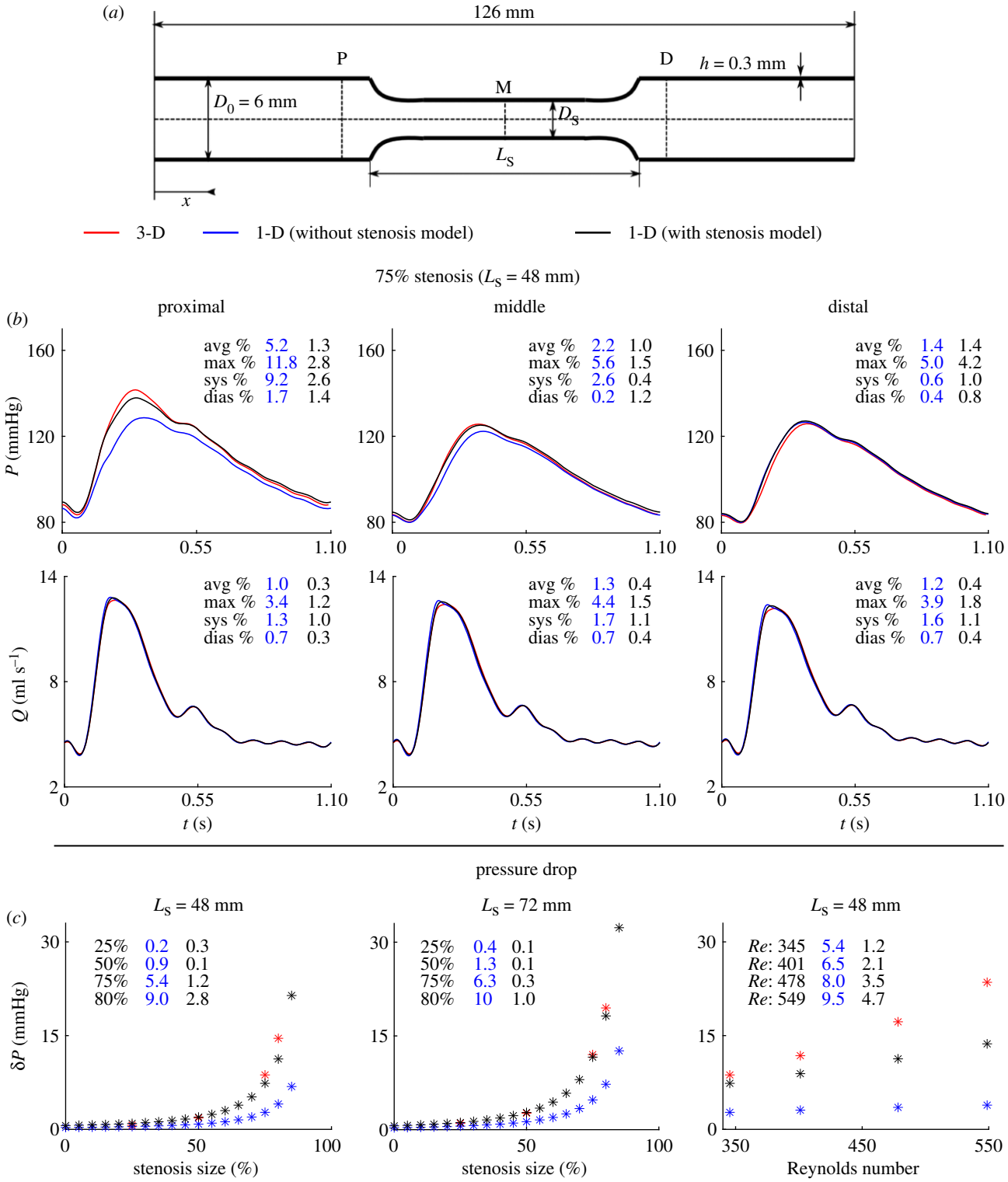

Figure 4. Results for the common carotid artery with a stenosis (1-D versus 3-D modelling). (*a*) The vascular geometry is characterized by the length of the stenosis, L_s, the initial, D_0, and stenosis, D_s, diameters and the wall thickness, h. (*b*) Pressure and flow rate with time at the proximal (P), middle (M) and distal (D) sides shown in panel (*a*), calculated using the 3-D model (red) and 1-D model, with (black) and without (blue) the stenosis model, for a 75%, 48-mm-long stenosis with a Reynolds number of 345. Average (avg), maximum (max), systolic (sys) and diastolic (dias) relative error metrics are shown in each panel (column 1: without stenosis model; column 2: with stenosis model). (c) Pressure drop, δP, from the proximal to distal side with stenosis size, for a 48-mm-long stenosis (left) and a 72-mm-long stenosis (middle), and with Reynolds number (right) for a 75%, 48-mm-long stenosis (right), for the 3-D model (red stars) and 1-D model with (black stars) and without (blue stars) the stenosis model. 3-D model results shown for a few cases only. Relative errors $\epsilon_{\delta P}$ calculated by equation (2.9) with (column 1) and without (column 2) the stenosis model are shown in each panel.

diastole. For all cases studied, all relative errors defined in §2.3 for pressure and flow waves were considerably smaller when the stenosis model was used, in particular for the pressure wave in sites proximal to the stenosis (e.g. $\leq$1.3% versus $\leq$5.2% for the 75%, 48-mm-long stenosis case).

Comparisons between 1-D and 3-D pulse waves for all cases simulated in this study (i.e. for different stenosis sizes and lengths, and *Re*) are provided in electronic supplementary material, figures S1–S5. Relative errors for both pressure and the flow increased with the increasing stenosis

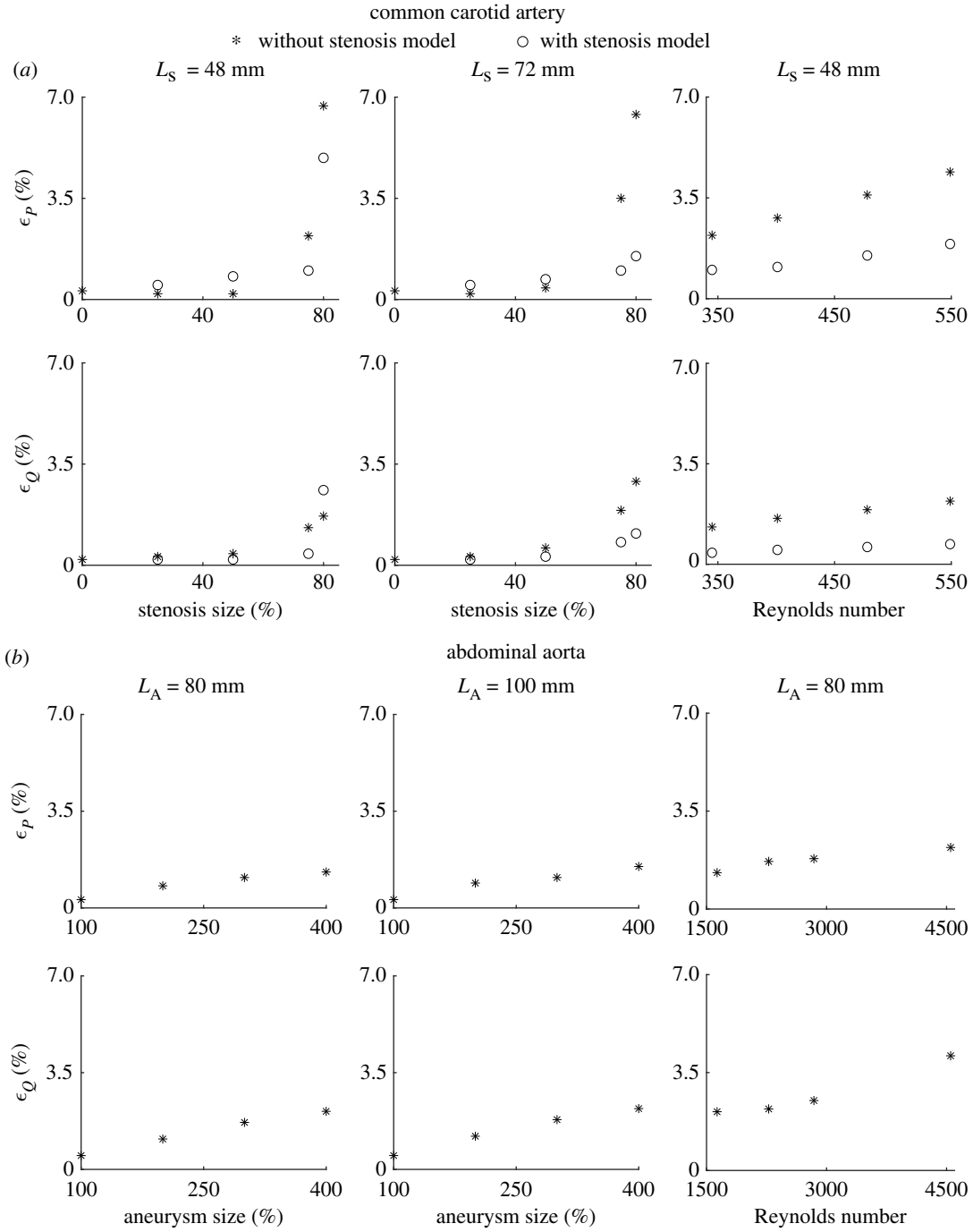

Figure 5. Relative RMSEs for the common carotid artery (*a*) and abdominal aorta (*b*). (*a*) Errors for blood pressure, ϵ_P, and flow, ϵ_Q, in the middle side with stenosis size, for a 48-mm-long stenosis (left) and a 72-mm-long stenosis (middle), and with Reynolds number for a 75%, 48-mm-long stenosis (right). Relative errors are provided for the 1-D model with (circles) and without (stars) the stenosis model. (*b*) ϵ_P and ϵ_Q in the middle side with aneurysm size, for 80-mm-long (left) and 100-mm-long (middle) aneurysms, and with Reynolds number for a 400%, 80-mm-long aneurysm (right).

size, decreasing stenosis length and increasing *Re*. Moreover, discrepancies in both pressure and flow predictions occur mainly in systole, leading to greater systolic than diastolic relative errors, as well as maximum relative errors usually occurring within systole. Figure 5*a* shows ϵ^{RMS} at the middle of the stenosis for all cases simulated in this study. Overall, these were smaller when using the stenosis model, leading to ϵ^{RMS} smaller than 4.9% for pressure and 2.6% for the flow for all cases studied, with the greatest ϵ^{RMS} obtained for the case with an 80%, 48-mm-long stenosis and $Re = 345$.

The pressure drop across the stenosis, δP, increased with increasing stenosis size and length, and increasing *Re* (figure 4*c*). The relative error metric $\epsilon_{\delta P}$ used to quantify the accuracy of the 1-D model estimate of δP increased with increasing stenosis size and *Re* and decreasing stenosis length, with the maximum absolute error for δP being 9.8 mmHg (figure 4*c*, $Re = 549$). Furthermore, the stenosis model reduced $\epsilon_{\delta P}$ considerably: $\epsilon_{\delta P} \leq 10.0\%$ versus $\leq 4.7\%$ for all cases studied.

3.1.2. Abdominal aorta with an aneurysm

Figure 6*b* shows 1-D model predictions for pressure and flow waves at 5 mm proximal, the middle and 5 mm distal to a 400%, 80-mm-long aneurysm, together with corresponding 3-D results. At those sites, ϵ^{RMS} remained smaller than 1.6% for pressure waves and 7.3% for flow waves when an AAA of up to 400% in size was present in the middle of the vessel, for a physiological *Re* of 1632. The 1-D model

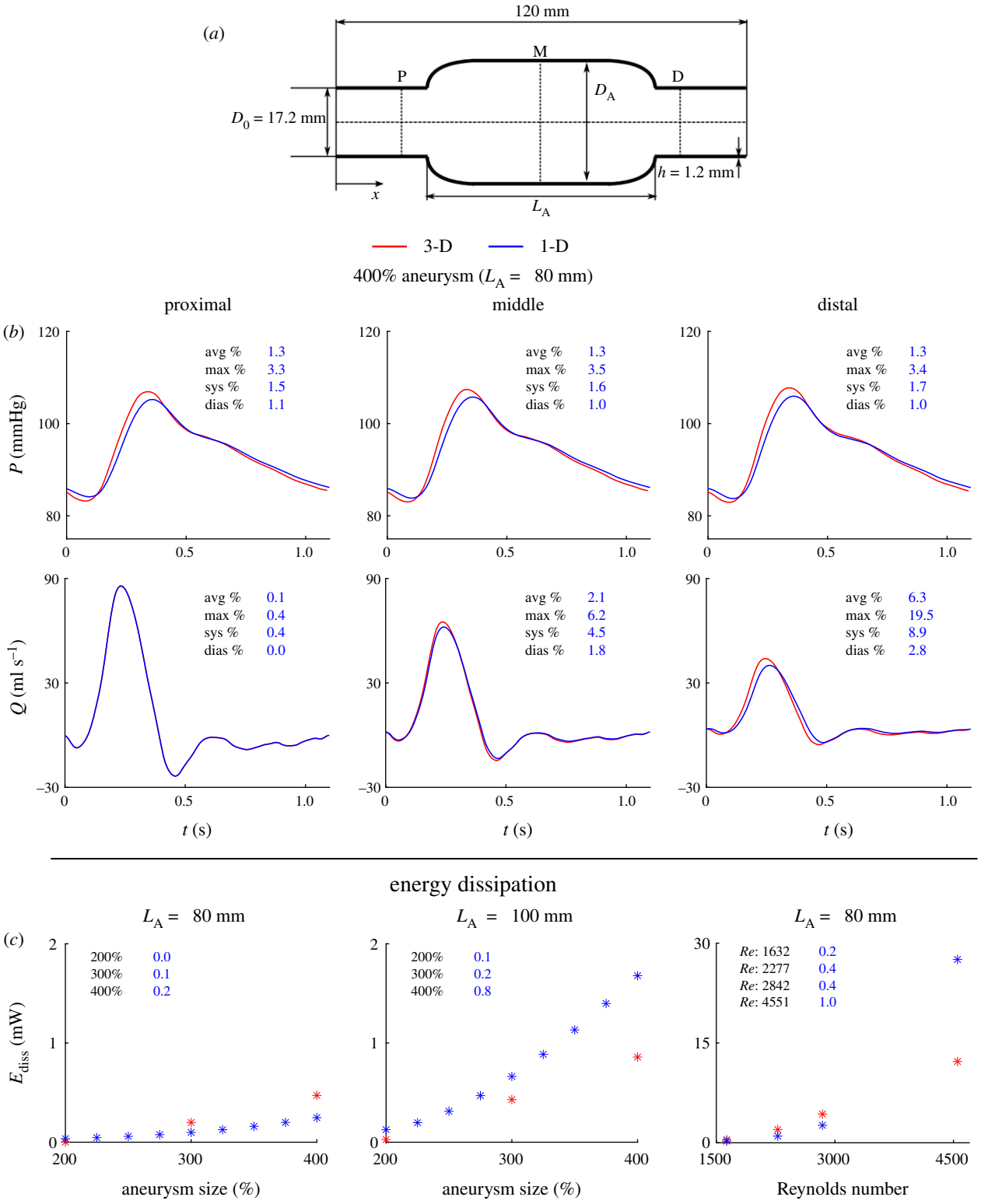

Figure 6. Results for the abdominal aorta with an aneurysm (1-D versus 3-D modelling). (*a*) The vascular geometry is characterized by the length of the aneurysm, L_A, the initial, D_0, and aneurysm, D_A, diameters and the wall thickness, h. (*b*) Pressure and flow rate with time at the proximal (P), middle (M) and distal (D) sides shown in panel (a), calculated using the 3-D model (red) and 1-D model (blue) for a 400%, 80-mm-long aneurysm with a Reynolds number of 1632. Average (avg), maximum (max), systolic (sys) and diastolic (dias) relative error metrics are shown in each panel. (c) Energy dissipation, E_{diss}, from the proximal to distal side with aneurysm size, for an 80-mm-long (left) and a 100-mm-long (middle) aneurysm, and with Reynolds number for a 400%, 80-mm-long aneurysm (right; note the change in the y-axis scale). Relative errors, $\epsilon_{E_{diss}}$, calculated by equation (2.11) are shown in each panel for the cases in which 3-D model results were available.

formulation was able to capture the main features of both pressure and flow waveforms produced by the 3-D formulation. Relative errors in blood pressure were smaller, and relative errors in blood flow were larger, than those obtained for the CCA with a stenosis. For all cases, 1-D modelling was able to reproduce the decrease in flow amplitude towards distal locations—which was more prominent with the increasing aneurysm size and length—while maintaining mean blood flow and pulse pressure constant along the blood vessel. In addition, the 1-D formulation was able to capture the decrease in pulse pressure along the vessel with increasing aneurysm size. 1-D model predictions

systematically underestimated the amplitude of 3-D model pressure and flow waves, though relative errors in systolic and diastolic pressure were smaller than 2.2% and 1.1%, respectively, whereas relative errors in systolic and diastolic flow were smaller than 9.0% and 3.9%, respectively.

Electronic supplementary material, figures S6–S8 show all the 1-D versus 3-D comparisons for pressure and flow waveforms that were studied for the abdominal aorta case. All relative error metrics increased with increasing aneurysm size and length, and increasing *Re*. As in the CCA case, discrepancies in both pressure and flow predictions occurred mainly in systole rather than in diastole. Relative errors for pressure were similar throughout the vessel, but relative errors for the flow increased from inlet to outlet. For all the cases simulated in this study, ϵ^{RMS} in the middle of the aneurysm was less than 2.2% for pressure and 4.1% for flow, with the greatest values of ϵ^{RMS} corresponding to a 400%, 80-mm-long aneurysm with $Re = 4551$ (figure 5*b*). In addition, both the energy dissipation, E_{diss}, and the relative error metric, $\epsilon_{E_{\mathrm{diss}}}$, used to quantify the accuracy of E_{diss} calculated by the 1-D model increased with increasing aneurysm size and length, and with increasing *Re*, with the maximum absolute error for E_{diss} being 15.3 mW (figure 6*c*, $Re = 4551$). $\epsilon_{E_{\mathrm{diss}}}$ values were 0.2% or less for an aneurysm length of 80 mm, and increased to 0.8% or less when the aneurysm length increased to 100 mm, and further increased to 1.0% or less when the *Re* increased from 1632 to 4551.

3.1.3. Aortic bifurcation with a stenosis and an aneurysm

The stenosis model was used in all 1-D simulations of the aortic bifurcation since, when this model was used, previous results had shown a considerable decrease in relative errors for both pulse wave morphology and pressure drop across the stenosis. The 1-D formulation with the stenosis model was able to reproduce the morphology of 3-D model pressure and flow waveforms accurately when adding an 85%, 60-mm-long stenosis to the left iliac artery of the aortic bifurcation model (figure 7*a*). ϵ^{RMS} for pressure and flow waves in the middle of the three vessels of the aortic bifurcation were, respectively, less than 1.0% and 4.2%. 1-D versus 3-D comparisons of pressure and flow waveforms are provided for the middle point of the three vessels (figure 7*b*) and at their inlets and outlets (electronic supplementary material, figure S10). Pressure ϵ^{RMS} values were similar to those obtained for the CCA with an 80%, 72-mm-long stenosis (2.2% or less; see electronic supplementary material, figure S4, bottom), and considerably smaller than the 80%, 48-mm-long stenosis case (5.4% or less; electronic supplementary material, figure S2, bottom). Flow ϵ^{RMS} values were slightly larger than those obtained for the CCA with an 80% stenosis, both 48 and 72 mm long (3% or less). Furthermore, 1-D modelling was able to simulate the pressure drop across the stenosis in the left iliac artery with a relative error of $\epsilon_{\delta P} = 0.5\%$, which is smaller than the corresponding values obtained for the CCA with an 80%, 48-mm-long stenosis (2.8%) and an 80%, 72-mm-long stenosis (1.0%).

Adding a 300%, 80-mm-long AAA to the aortic bifurcation model with an 85%, 60-mm-long stenosis in the left iliac artery increased the ϵ^{RMS} value to 7.3% or less in the middle of the three vessels of the aortic bifurcation reported above for the flow wave (figure 7*c*). However, the 1-D formulation was still able to capture the decrease in pulse pressure in the three vessels observed in the 3-D results and maintain $\epsilon^{\mathrm{RMS}} \leq 2.0\%$ for pressure, despite increasing systolic and diastolic relative errors from 1.0% or less to 2.0% or less. 1-D versus 3-D pressure and flow waveforms at the inlets and outlets are shown in electronic supplementary material, figure S11. The increases in flow and pressure relative errors were caused by an underestimation of the amplitude of 3-D model pressure and flow waves, as observed for the abdominal aorta case with an AAA (figure 7*c*). Furthermore, $\epsilon_{\delta P}$ across the stenosis in the left iliac artery remained almost unchanged compared with the case without an AAA (0.8% versus 0.5%). The 1-D formulation was able to estimate the energy dissipation across the AAA with a relative error of $\epsilon_{E_{\mathrm{diss}}} = 0.1\%$, which was smaller than the values obtained for the same size AAA in the abdominal aorta case.

For both cases, discrepancies in both pressure and flow predictions occurred mainly in systole rather than in diastole. Moreover, the greater relative errors for pressure waves were obtained in the middle of the stenosis and, for the second case, in the middle of the AAA as well. For example, ϵ^{RMS} increased up to 1.6% for pressure and 7.3% for the flow compared with the 0.7% or less and 1.7% or less errors, respectively, obtained for the baseline simulation (electronic supplementary material, figure S9).

3.2. Assessment against *in vitro* measurements

Young's modulus measured on five specimens of the abdominal aorta phantoms by the electromechanical test system was 690 ± 23 kPa. Figure 8 shows the pressure measured *in vitro* and simulated by the 1-D model at the inlet, middle and outlet of the three phantoms using this Young's modulus. The thick red and blue lines are, respectively, the ensemble-average pressure waveforms from the *in vitro* measurements and simulated using the 1-D model. For the *in vitro* measurements, the shaded areas indicate the ensemble standard deviation of the pressure wave. The shaded areas of the 1-D model pressures were obtained as follows. Ensemble-averaged inflow boundary condition and mean Young's modulus were used to simulate the ensemble-averaged pressure wave; ensemble-averaged inflow ± standard deviation and mean Young's modulus ± standard deviation were used to simulate the upper and lower pressure values of the shaded areas.

The 1-D formulation was able to reproduce the *in vitro* pressure waves with average, systolic and diastolic relative errors smaller than 5.0% for all three cases. These errors were larger than corresponding errors obtained by comparison against 3-D model pressures (2.0% or less). Unlike in the comparisons against 3-D model pressures, relative errors were not affected by the aneurysm size and increased with the distance from the inlet. 1-D modelling was able to capture the decrease in pulse pressure with increasing aneurysm size observed *in vitro*, which was also observed in the 3-D model pressures. Overall, ϵ^{RMS} values were similar along the three aortic phantom geometries, which is consistent with the results obtained when comparing against the 3-D model pressures.

4. Discussion

We have tested the accuracy of 1-D model pressure and flow waveforms in a series of idealized vascular geometries representing the abdominal aorta, common carotid and iliac arteries with different sizes of stenoses and/or aneurysms.

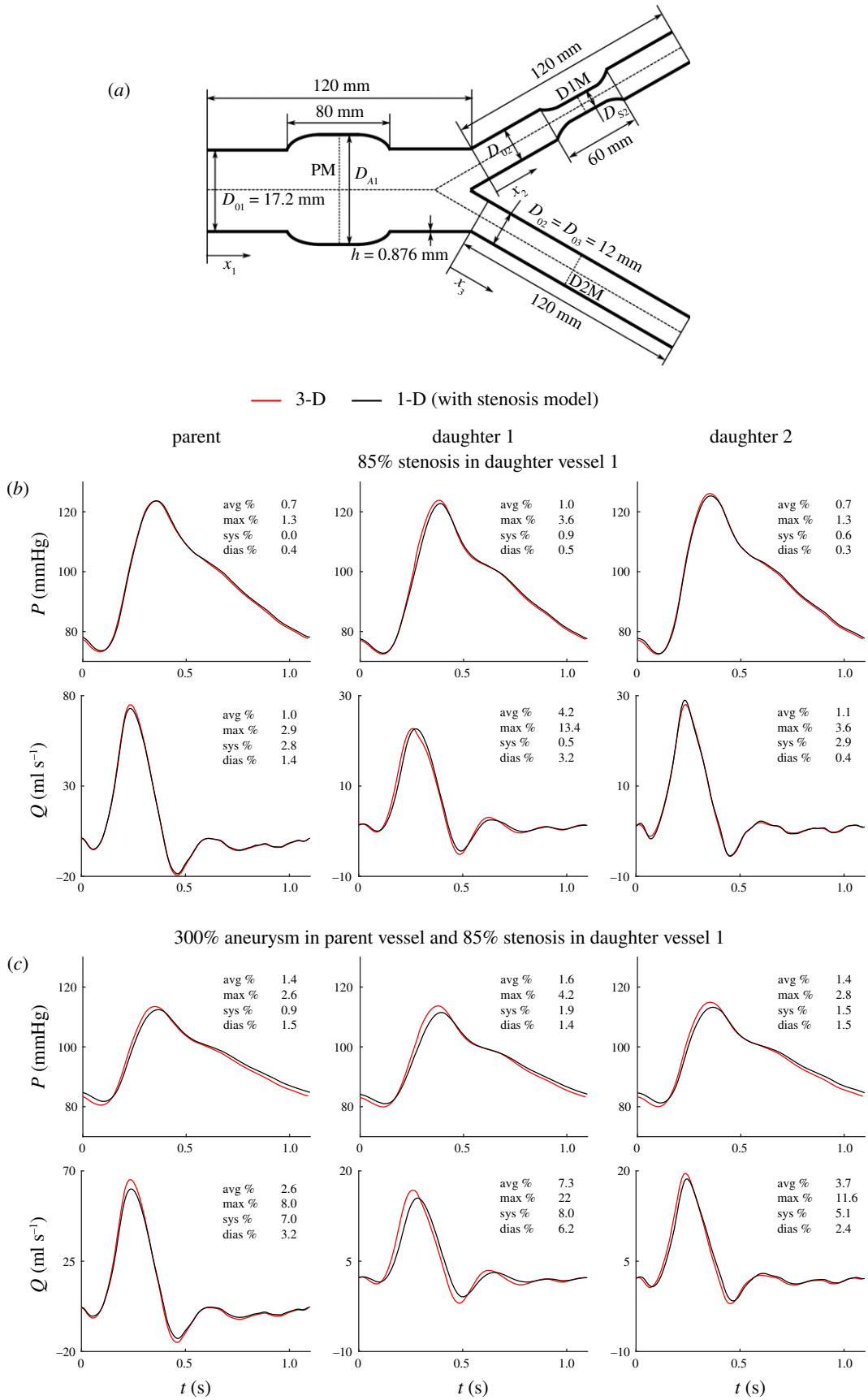

Figure 7. Results for the aortic bifurcation with an aneurysm in the parent vessel and a stenosis in daughter vessel 1 (1-D versus 3-D modelling). (*a*) The vascular geometry is characterized by the initial, D_{01}, D_{02}, D_{03}, aneurysm, D_{A1}, and stenosis, D_{s2}, diameters and wall thickness, h. (*b*) Pressure and flow rate with time in the middle of the three vessels as indicated in panel (*a*), calculated using the 3-D model (red) and 1-D model (black) with an 85% stenosis in the middle of daughter vessel 1 (top) and a 300% aneurysm in the middle of the parent vessel together with an 85% stenosis in the middle of daughter vessel 1 (bottom). Average (avg), maximum (max), systolic (sys) and diastolic (dias) relative error metrics are shown in each panel.

These arteries were selected for being preferable locations for aneurysm or stenosis in large vessels [57,58]. This is the first attempt, to our knowledge, to test systematically and quantitatively the accuracy of the 1-D formulation in arteries with localized changes in luminal cross-sectional area due to the presence of vascular disease. Overall, we have shown that

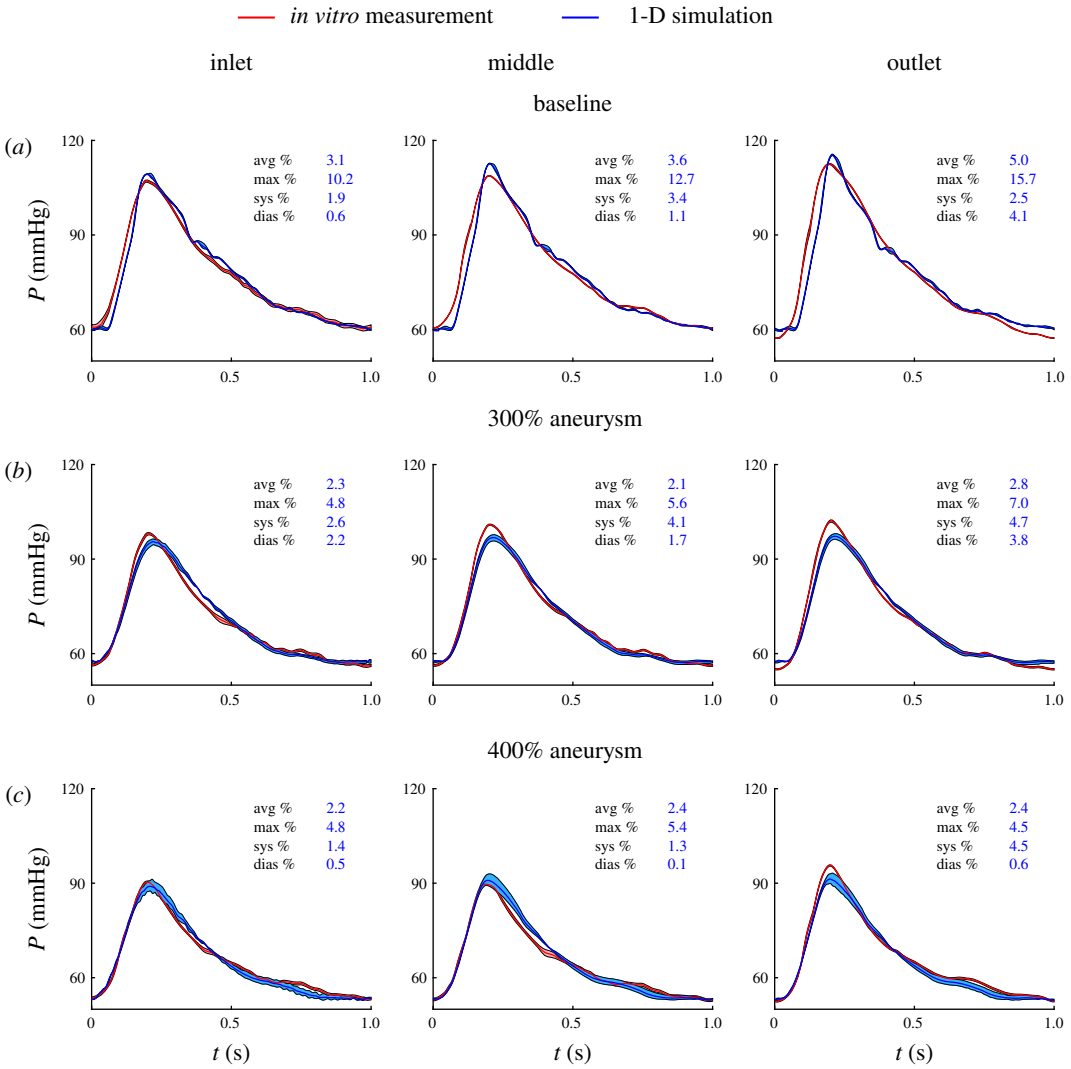

Figure 8. Results for the abdominal aorta with an aneurysm (1-D versus *in vitro* modelling). Pressure with time measured *in vitro* (red) and simulated by the 1-D model (blue) at the inlet, middle and outlet of the vessel for the baseline (*a*), 300% aneurysm (*b*) and 400% aneurysm (*c*) geometries. The plots also show the standard deviation (shaded areas) of the ensemble average of each *in vitro* and simulated pressure wave. Average (avg), maximum (max), systolic (sys) and diastolic (dias) relative error metrics are shown in each panel.

1-D modelling is able to reproduce the main features of pressure and flow waves, pressure drop across the stenoses and energy dissipation across aneurysms observed in the 3-D models that were used as the ground truth. Under physiological Reynolds numbers (*Re*), relative RMSEs were smaller than 5.4% for pressure and 7.3% for the flow in the vessels studied, for stenosis and AAA sizes of up to 85% and 400%, respectively. The errors are slightly larger than corresponding relative errors previously reported for the aorta and other large arteries with normal vascular geometries, in which relative RMSEs smaller than 2.1% and 5.0%, respectively, were obtained when also using 3-D model data as the ground truth (table 1). We have also shown the ability of 1-D modelling to simulate pressure waves acquired from phantoms of the abdominal aorta, leading to relative RMSE values of 5.0% or less, which are comparable to those obtained in previous studies (10.0% or less) for which *in vitro* data were used as the ground truth. Our study provides additional support for the use of 1-D modelling to accurately simulate pressure and flow waves in large diseased arteries with a reasonable computational cost. Moreover, all the 1-D, 3-D and *in vitro* data from this study are available online, providing a comprehensive reference dataset to support the development of 1-D models and numerical schemes in diseased arterial vasculatures.

We first discuss the effect of a stenosis and/or aneurysm on 1-D model pressure and flow waves, and then the limitations and significance of our results.

4.1. Stenosis

The primary source of discrepancies between 1-D and 3-D model pulse waves across a stenosis was underestimation by 1-D modelling of the pressure loss across the stenosis. Using 3-D modelling, complex flow patterns and increased wall shear stresses can be observed around a stenosis region [59–62]. These complex flow phenomena cannot be described by the 1-D formulation, which led to relative errors in pressure and flow waves that increased with increasing stenosis size. Moreover, relative errors were considerably greater for pressure than for flow in the CCA case, especially at locations proximal to the stenosis. This is because the mean flow rate and, to a large extent, flow wave patterns were determined by the inflow boundary condition and preserved throughout the vessel according to the law of conservation of mass (equation (2.1)). Instead, the pressure gradient required to drive the prescribed inflow waveforms increased with the increasing pressure drop across the stenosis (this drop got larger with increasing

stenosis size, length and *Re*), leading to greater pressures in proximal locations. Pressures in distal locations were determined by the outflow boundary condition, which was identical in both 1-D and 3-D formulations, leading to much smaller relative errors in pressure.

By introducing an empirically based stenosis model—accounting for the pressure loss across the stenosis—into the 1-D formulation of the CCA case with stenoses larger than 50% in size, relative errors were overall considerably reduced; for example, relative RMSE decreased from a maximum of 10.6% in pressure and 3.2% in flow to a maximum of 2.2% and 1.6%, respectively, in an 80%, 72-mm-long stenosis. Moreover, pressure drops across the stenosis, δP, were remarkably better reproduced: the maximum value of the relative error metric $\epsilon_{\delta P}$ used to quantify the accuracy of the 1-D model estimate of δP was at least halved and decreased by up to 90% in some cases.

Comparing the aortic bifurcation and CCA cases, relative errors for the pressure were considerably smaller in the aortic bifurcation case with an 85% stenosis in the iliac artery than in the CCA case with an 80% stenosis. This is in agreement with the increase in relative pressure errors with increasing Reynolds number (*Re*) observed in the CCA case. Indeed, under normal physiological *Re*, the iliac *Re* was smaller than the CCA *Re* (*Re* = 106 versus 345). Furthermore, relative errors in pressure were similar throughout the vessels of the aortic bifurcation case, since proximal pressures did not increase with the presence of the stenosis to drive the prescribed inflow. This is because volume flow rates could be redistributed towards the iliac artery without the stenosis, which provided less resistance to blood flow. In fact, the flow distribution between the iliac artery with and without stenosis,changed considerably, especially during systole (peak flow rates in the middle of the iliac arteries were 25 ml s^{-1} and 29 ml s^{-1}, respectively). The systolic flow split in the two iliac arteries was slightly different in 1-D and 3-D modelling (46.2/53.8% in 1-D versus 45.1/54.9% in 3-D), leading to larger relative errors in 1-D model flows than in the CCA case.

In general, the largest differences between 1-D and 3-D model pressures and flows in the two cases with a stenosis occurred in systole, whereas the diastolic predictions were much closer, in agreement with previous results obtained in healthy vasculatures [11,19]. Systolic flow is fundamentally nonlinear and advection/inertia-dominated, and, therefore, larger differences between the two formulations were observed as expected. Conversely, the physics of blood flow becomes increasingly linear and inertia-free with increasing time in diastole, facilitating the task of the 1-D formulation to reproduce pressure and flow waves in diastole [63].

The empirically based stenosis model used in this study originated from the *in vivo* experiments in dogs by Young *et al.* [34] and *in vitro* measurements by Seeley & Young [35]. In those experiments a range of stenoses from 50% to over 90% in size, 6.5 mm to 101.4 mm in length, and *Re* from less than 100 to over 1000 were considered under pulsatile and steady flow conditions. We have shown that 1-D modelling with this stenosis model can provide pulse waveforms much closer to the 3-D model waveforms in stenosis sizes from 50% to up to 85%, stenosis lengths from 48 mm to 72 mm, and $Re \leq 550$, which are within the corresponding ranges of values considered in the *in vivo* and *in vitro* experiments.

4.2. Aneurysm

The primary cause of relative errors in the aneurysm model was the inability of 1-D modelling to describe the intricate 3-D flow patterns inside the aneurysm, which can be observed in 3-D model simulations [9,64,65]. As a result, relative errors were considerably greater for the flow than for the pressure when an AAA was present, in both the abdominal aorta and aortic bifurcation cases. Unlike in the CCA case with a stenosis, the pressure gradient required to drive the prescribed inflow in the abdominal aorta case was not significantly affected by the presence of the AAA and, hence, relative errors in pressure stayed low and varied little along the vessel. On the other hand, relative errors in the flow increased towards distal locations and with increasing AAA size and length. Furthermore, flow waves were determined by the inflow boundary condition in locations proximal to the AAA, and were affected by the size and length of the AAA in distal locations. With increasing AAA size and length, more flow was stored in the AAA region in systole, resulting in the aneurysm region expanding and further increasing vascular compliance, which is directly proportional to the luminal cross-sectional area [50]. In the 3-D models, the external tissue support reduced the expansion of the aneurysm region, leading to smaller compliances and, hence, the Windkessel effect was greater in the 1-D simulations. As a result, pulse pressures and flow amplitudes were greater in the 3-D than in the 1-D simulations, with their differences increasing with increasing AAA size and length.

The interplay between the presence of a stenosis and an aneurysm was studied in the abdominal aortic bifurcation case. Adding an AAA to the aortic bifurcation model with an 85% iliac artery stenosis increased relative errors, especially in the flow. The presence of the aneurysm increased compliance in the vasculature, especially in the 1-D model that was without tissue support. The additional compliance in the abdominal aorta decreased the amplitude of the blood pressure and flow towards the outlet of the aorta. As a result, the pressure and flow amplitudes in the left iliac artery with a stenosis also decreased, leading to larger relative errors when both a stenosis and an aneurysm were present.

We have used the energy dissipation across the AAA (the difference in energy flux between a proximal and a distal location) to evaluate the ability of 1-D modelling to account for the effect on pressure and flow waves of the intricate 3-D flow patterns within the AAA. This dissipation metric was proposed in the study by Marsden *et al.* [56] and takes into account changes in both blood flow and pressure between several vascular locations. In general, our results have shown that 1-D modelling can provide both accurate pulse waveforms and energy dissipations for aneurysm sizes up to 400% and $Re \leq 4551$.

The maximum relative RMSEs obtained when testing the 1-D formulation against the *in vitro* measurements were slightly larger than the RMSEs found when assessing 1-D modelling against 3-D modelling (5% or less versus 2.7% or less). This is in agreement with the results presented in previous studies comparing 1-D versus *in vitro* and 3-D data, as shown in table 1. In addition, the relative errors in pressure varied little with increasing size of the aneurysm, similar to the results found when comparing 1-D and 3-D simulations: the maximum difference in the relative RMSEs between a

300% and a 400% aneurysm was 0.4%. In our study, the measured and simulated pressure waves did not show the oscillations observed in the study performed by Sazonov *et al.* [38]. A possible reason for this is the greater Young's modulus used in Sazonov *et al.*'s study, which was about four times larger than that used in this study, resulting in decreased compliance in the experimental vasculature; however, further investigations are required to confirm this. Another possible reason for the oscillation-free measurement results found in our study is the presence of water filling the gap between the phantom and the rigid experimental table, which prevented any resonance from occurring between the phantom and the rigid table.

4.3. Limitations

In vivo data were not used in this study as the ground truth. Instead, 3-D model and experimental data were used, which have the fundamental advantage of reducing the uncertainty of the 1-D model physical parameters. The 1-D and 3-D formulations shared identical boundary conditions and had equivalent vascular geometries and material properties. Relatively accurate measurements of the physical parameters used in the 1-D models of the abdominal aorta phantoms were possible for all parameters except for fluid density and viscosity. In this study, therefore, we have shown that the 1-D formulation is able to capture the main features of pressure and flow waves across stenoses/aneurysms in large vessels with reasonable accuracy, provided that accurate measurements of all physical parameters are used. As a result, this study provides a theoretical lower bound of relative errors to be expected when testing 1-D modelling against *in vivo* data.

We have investigated a particular numerical implementation of the 1-D model theory, which accounts for nonlinear effects and is able to provide physiological features of human pulse waveforms in normal vasculatures [66]. More complex 1-D formulations than the one considered here have been proposed, for example those accounting for wall visco-elasticity [13], space-varying and time-varying velocity profiles [16,67] and highly nonlinear terms [16,68]. However, assessing all these formulations was beyond the scope of this study. Furthermore, laminar flow was assumed in both 1-D and 3-D model simulations. This approach fits most of the simulation cases for which the Reynolds numbers (at peak flow velocity) were smaller than 2100. However, some extreme cases in which the Reynolds number went up to 4561 may benefit from using turbulent flow models.

The low relative errors obtained in this study are comparable to those obtained in other studies involving normal arterial geometries (e.g. those listed in table 1). They should, however, be confirmed in patient-specific geometries with anatomically correct stenoses and/or aneurysms and in arterial tree models with the larger systemic arteries simulated using 1-D modelling.

Lastly, the impact of neglecting energy losses at the aortic bifurcation has not been analysed, although it should be insignificant because of the small relative errors obtained in the aortic bifurcation case. This is in agreement with the findings of previous studies [11,12]. The impact of other geometrical features such as tapering, curvature and torsion has not been studied here, but it has been previously shown to also be insignificant and affecting mainly 3-D flow patterns rather than pulse wave morphologies [11].

4.4. Significance

This study was motivated by the scarceness of test cases for benchmarking 1-D numerical schemes in diseased vasculatures and our desire to provide an accessible reference dataset. Previous studies have used 1-D modelling to study pulse wave propagation across stenoses [69,70] and aneurysms [38], before having comprehensively verified 1-D modelling in such diseased vasculatures. Our results suggest that 1-D modelling offers a good balance between accuracy and computational cost in arteries with localized changes in luminal cross-sectional area, supporting the use of 1-D modelling in those previous studies on diseased vasculatures, and in future studies. We have shown that discrepancies in both pressure and flow predictions obtained by using 3-D and *in vitro* data as the ground truth are similar to those obtained in the studies shown in table 1 that also tested 1-D modelling in normal vascular geometries using 3-D model and *in vitro* reference data. Moreover, we have shown that the 1-D formulation is inexpensive to compute in diseased vasculatures compared with the 3-D formulation (minutes versus days).

Having a robust and fast 1-D formulation that is able to simulate arterial haemodynamics in diseased vasculatures will allow us to investigate indices and algorithms that can be obtained from pulse wave analysis and which may enable early detection of stenoses and AAA. In addition to existing indices, such as fractional flow reserve for coronary artery stenosis [71,72], new indices, such as the energy dissipation across an AAA proposed in this study, can be assessed using 1-D modelling under a wide range of cardiovascular conditions, which is currently prohibitive—from a computational standpoint—when using 3-D modelling. Moreover, our results support the use of 1-D modelling to create datasets of thousands of 'virtual' (computed) subjects with different sizes of large-artery stenoses and AAA for assessing the performance of such indices and algorithms, following our existing approach [73], which so far has been used to create healthy virtual subjects only. For instance, deep-learning algorithms for estimating the size of an AAA from a peripheral pressure wave can be developed using such datasets of virtual subjects [74].

5. Conclusion

We have shown the ability of the 1-D formulation—with an empirical model of energy losses across stenoses—to capture the main features of pressure and flow waveforms in the CCA with stenoses of up to 85% in size, the abdominal aorta with aneurysms of up to 400% in size and the abdominal aorta with an AAA of 300% in size and an iliac stenosis of 85% in size. This study provides additional support for the use of 1-D modelling to accurately simulate pressure and flow waves in large diseased arteries with a reasonable computational cost. All numerical and experimental data generated in this study are freely available and are a valuable resource for future research.

Data accessibility. Additional data are included in the electronic supplementary material.

Competing interests. We declare we have no competing interests.

Funding. This work was supported by the British Heart Foundation (BHF) (grant no. PG/15/104/31913), the EPSRC (grant no. EP/K031546/1), the Wellcome/Engineering Physical Sciences Research

Council (EPSRC) Centre for Medical Engineering at King's College London (grant no. WT 203148/Z/16/Z), the Department of Health through the National Institute for Health Research (NIHR) Cardiovascular MedTech Co-operative at Guy's and St Thomas' NHS Foundation Trust (GSTT), the comprehensive Biomedical Research Centre and Clinical Research Facilities awards to GSTT in partnership with King's College London and King's College Hospital NHS Foundation Trust, and the Ministry of Science and Higher Education of the Russian Federation within the framework of state support for the creation and development of World-Class Research Centers 'Digital biodesign and personalized healthcare' (075-15-2020-926). The views expressed are those of the authors and not necessarily those of the BHF, Wellcome Trust, EPSRC, NIHR, GSTT or Ministry of Science. W.J. was funded by a King's College London PGR International Scholarship.

Acknowledgements. The authors acknowledge Dr Christopher J. Arthurs for his excellent advice on how to use CRIMSON, all the CRIMSON team for making their software available to this project and the School of Biomedical Engineering and Imaging Sciences at King's College London for giving us access to their high-performance computer (Tom) to run all 3-D simulations.

References

1. Westerhof N, Lankhaar JW, Westerhof BE. 2009 The arterial Windkessel. *Med. Biol. Eng. Comput.* **47**, 131–141. (doi:10.1007/s11517-008-0359-2)
2. Olufsen MS, Ottesen JT, Tran HT, Ellwein LM, Lipsitz LA, Novak V. 2005 Blood pressure and blood flow variation during postural change from sitting to standing: model development and validation. *J. Appl. Physiol.* **99**, 1523–1537. (doi:10.1152/japplphysiol.00177.2005)
3. Magosso E, Ursino M. 2002 Cardiovascular response to dynamic aerobic exercise: a mathematical model. *Med. Biol. Eng. Comput.* **40**, 660–674. (doi:10.1007/BF02345305)
4. Jin W. 2016 Evaluating cardiac functions under exercise and postural change with a multi-physical model coupling cardiovascular and autonomic nervous systems. PhD thesis, Chiba University, Chiba, Japan.
5. Xiao N, Humphrey JD, Figueroa CA. 2013 Multi-scale computational model of three-dimensional hemodynamics within a deformable full-body arterial network. *J. Comput. Phys.* **244**, 20–40. (doi:10.1016/j.jcp.2012.09.016)
6. Schirmer CM, Malek AM. 2012 Computational fluid dynamic characterization of carotid bifurcation stenosis in patient-based geometries. *Brain Behav.* **2**, 42–52. (doi:10.1002/brb3.25)
7. Gallo D *et al*. 2018 Segment-specific associations between local haemodynamic and imaging markers of early atherosclerosis at the carotid artery: an *in vivo* human study. *J. R. Soc. Interface* **15**, 20180352. (doi:10.1098/rsif.2018.0352)
8. Poelma C, Watton PN, Ventikos Y. 2015 Transitional flow in aneurysms and the computation of haemodynamic parameters. *J. R. Soc. Interface* **12**, 20141394. (doi:10.1098/rsif.2014.1394)
9. Sharzehee M, Khalafvand SS, Han HC. 2018 Fluid-structure interaction modeling of aneurysmal arteries under steady-state and pulsatile blood flow: a stability analysis. *Comput. Methods Biomech. Biomed. Engin.* **21**, 219–231. (doi:10.1080/10255842.2018.1439478)
10. Taylor CA, Draney MT. 2004 Experimental and computational methods in cardiovascular fluid mechanics. *Annu. Rev. Fluid Mech.* **36**, 197–231. (doi:10.1146/annurev.fluid.36.050802.121944)
11. Xiao N, Alastruey J, Figueroa CA. 2014 A systematic comparison between 1-D and 3-D hemodynamics in compliant arterial models. *Int. J. Numer. Methods Biomed. Eng.* **30**, 204–231. (doi:10.1002/cnm.2598)
12. Matthys KS, Alastruey J, Peiró J, Khir AW, Segers P, Verdonck PR, Parker KH, Sherwin SJ. 2007 Pulse wave propagation in a model human arterial network: assessment of 1-D numerical simulations against in vitro measurements. *J. Biomech.* **40**, 3476–3486. (doi:10.1016/j.jbiomech.2007.05.027)
13. Alastruey J, Khir AW, Matthys KS, Segers P, Sherwin SJ, Verdonck PR, Parker KH, Peiró J. 2011 Pulse wave propagation in a model human arterial network: assessment of 1-D visco-elastic simulations against in vitro measurements. *J. Biomech.* **44**, 2250–2258. (doi:10.1016/j.jbiomech.2011.05.041)
14. Saito M, Ikenaga Y, Matsukawa M, Watanabe Y, Asada T, Lagrèe P-Y. 2011 One-dimensional model for propagation of a pressure wave in a model of the human arterial network: comparison of theoretical and experimental results. *J. Biomech. Eng.* **133**, 121005. (doi:10.1115/1.4005472)
15. Boileau E *et al.* 2015 A benchmark study of numerical schemes for one-dimensional arterial blood flow modelling. *Int. J. Numer. Methods Biomed. Eng.* **26**, 807–827.
16. Reymond P, Merenda F, Perren F, Rüfenacht D, Stergiopulos N. 2009 Validation of a one-dimensional model of the systemic arterial tree. *Am. J. Physiol. Heart Circ. Physiol.* **297**, H208–H222. (doi:10.1152/ajpheart.00037.2009)
17. Reymond P, Bohraus Y, Perren F, Lazeyras F, Stergiopulos N. 2011 Validation of a patient-specific one-dimensional model of the systemic arterial tree. *Am. J. Physiol. Heart Circ. Physiol.* **301**, H1173–H1182. (doi:10.1152/ajpheart.00821.2010)
18. Willemet M, Lacroix V, Marchandise E. 2013 Validation of a 1D patient-specific model of the arterial hemodynamics in bypassed lower-limbs: simulations against *in vivo* measurements. *Med. Eng. Phys.* **35**, 1573–1583. (doi:10.1016/j.medengphy.2013.04.012)
19. Alastruey J, Xiao N, Fok H, Schaeffter T, Figueroa CA. 2016 On the impact of modelling assumptions in multi-scale, subject-specific models of aortic haemodynamics. *J. R. Soc. Interface* **13**, 1–17. (doi:10.1098/rsif.2016.0073)
20. Steele BN, Wan J, Ku JP, Hughes TJR, Taylor CA. 2003 *In vivo* validation of a one-dimensional finite-element method for predicting blood flow in cardiovascular bypass grafts. *IEEE Trans. Biomed. Eng.* **50**, 649–656. (doi:10.1109/TBME.2003.812201)
21. Mynard JP, Penny DJ, Smolich JJ. 2014 Scalability and *in vivo* validation of a multiscale numerical model of the left coronary circulation. *Am. J. Physiol. Heart Circ. Physiol.* **306**, H517–H528. (doi:10.1152/ajpheart.00603.2013)
22. Bessems D, Giannopapa CG, Rutten MCM, van de Vosse FN. 2008 Experimental validation of a time-domain-based wave propagation model of blood flow in viscoelastic vessels. *J. Biomech.* **41**, 284–291. (doi:10.1016/j.jbiomech.2007.09.014)
23. Huberts W, Van Canneyt K, Segers P, Eloot S, Tordoir JHM, Verdonck P, van de Vosse FN, Bosboom EMH. 2012 Experimental validation of a pulse wave propagation model for predicting hemodynamics after vascular access surgery. *J. Biomech.* **45**, 1684–1691. (doi:10.1016/j.jbiomech.2012.03.028)
24. Avolio AP. 1980 Multi-branched model of the human arterial system. *Med. Biol. Eng. Comput.* **18**, 709–718. (doi:10.1007/BF02441895)
25. Stettler JC, Niederer P, Anliker M. 1981 Theoretical analysis of arterial hemodynamics including the influence of bifurcations—Part I: mathematical model and prediction of normal pulse patterns. *Ann. Biomed. Eng.* **9**, 145–164. (doi:10.1007/BF02363533)
26. Stettler JC, Niederer P, Anliker M, Casty M. 1981 Theoretical analysis of arterial hemodynamics including the influence of bifurcations—Part II: critical evaluation of theoretical model and comparison with noninvasive measurements of flow patterns in normal and pathological cases. *Ann. Biomed. Eng.* **9**, 165–175. (doi:10.1007/BF02363534)
27. Olufsen MS, Peskin CS, Kim WY, Pedersen EM, Nadim A, Larsen J. 2000 Numerical simulation and experimental validation of blood flow in arteries with structured-tree outflow conditions. *Ann. Biomed. Eng.* **28**, 1281–1299. (doi:10.1114/1.1326031)
28. Strocchi M, Contarino C, Zhang Q, Bonmassari R, Toro EF. 2017 A global mathematical model for the simulation of stenoses and bypass placement in the human arterial system. *Appl. Math. Comput.* **300**, 21–39.
29. Mynard JP, Nithiarasu P. 2008 A 1D arterial blood flowmodel incorporating ventricular pressure, aortic

valve and regional coronary flowusing the locally conservative Galerkin (LCG) method. *Commun. Numer. Methods Eng.* **24**, 367–417. (doi:10.1002/cnm.1117)

30. Grinberg L, Cheever E, Anor T, Madsen JR, Karniadakis GE. 2011 Modeling blood flow circulation in intracranial arterial networks: a comparative 3D/1D simulation study. *Ann. Biomed. Eng.* **39**, 297–309. (doi:10.1007/s10439-010-0132-1)
31. Stergiopulos N, Young DF, Rogge TR. 1992 Computer simulation of arterial flow with applications to arterial and aortic stenoses. *J. Biomech.* **25**, 1477–1488. (doi:10.1016/0021-9290(92)90060-E)
32. Stergiopulos N, Spiridon M, Pythound F, Meister J-J. 1996 On the wave transmission and reflection properties of stenoses. *J. Biomech.* **29**, 31–38. (doi:10.1016/0021-9290(95)00023-2)
33. Wan J, Steele B, Spicer SA, Strohband S, Feijóo GR, Hughes TJR, Taylor CA. 2002 A one-dimensional finite element method for simulation-based medical planning for cardiovascular disease. *Comput. Methods Biomech. Biomed. Engin.* **5**, 195–206. (doi:10.1080/10255840290010670)
34. Young DF, Cholvin NR, Roth AC. 1975 Pressure drop across artificially induced stenoses in the femoral arteries of dogs. *Circ. Res.* **36**, 735–743. (doi:10.1161/01.RES.36.6.735)
35. Seeley BD, Young DF. 1976 Effect of geometry on pressure losses across models of arterial stenosis. *J. Biomech.* **9**, 439–448. (doi:10.1016/0021-9290(76)90086-5)
36. Papadakis G, Raspaud J. 2019 Wave propagation in stenotic vessels; theoretical analysis and comparison between 3D and 1D fluid-structure-interaction models. *J. Fluids Struct.* **88**, 352–366. (doi:10.1016/j.jfluidstructs.2019.06.003)
37. Safaei S. 2015 Simulating blood flow in an anatomical arterial network. PhD thesis, The University of Auckland, Auckland, New Zealand.
38. Sazonov I, Khir AW, Hacham WS, Boileau E, Carson JM, van Loon R, Ferguson C, Nithiarasu P. 2017 A novel method for non-invasively detecting the severity and location of aortic aneurysms. *Biomech. Model. Mechanobiol.* **16**, 1225–1242. (doi:10.1007/s10237-017-0884-8)
39. Swillens A, Lanoye L, De Backer J, Stergiopulos N, Verdonck PR, Vermassen F, Segers P. 2008 Effect of an abdominal aortic aneurysm on wave reflection in the aorta. *IEEE Trans. Biomed. Eng.* **55**, 1602–1611. (doi:10.1109/TBME.2007.913994)
40. Formaggia L, Nobile F, Quarteroni A, Veneziani A. 1999 Multiscale modelling of the circulatory system: a preliminary analysis. *Comput. Vis. Sci.* **2**, 75–83. (doi:10.1007/s007910050030).
41. Passerini T, de Luca M, Formaggia L, Quarteroni A, Veneziani A. 2009 A 3D/1D geometrical multiscale model of cerebral vasculature. *J. Eng. Math.* **64**, 319–330. (doi:10.1007/s10665-009-9281-3)
42. Quarteroni A, Veneziani A, Vergara C. 2016 Geometric multiscale modeling of the cardiovascular system, between theory and practice. *Comput. Methods Appl. Mech. Eng.* **302**, 193–252. (doi:10.1016/j.cma.2016.01.007)
43. Yu H, Huang GP, Yang Z, Ludwig BR. 2018 A multiscale computational modeling for cerebral blood flow with aneurysms and/or stenoses. *Int. J. Numer. Methods Biomed. Eng.* **34**, 1–14.
44. Taelman L, Degroote J, Verdonck P, Vierendeels J, Segers P. 2013 Modeling hemodynamics in vascular networks using a geometrical multiscale approach: numerical aspects. *Ann. Biomed. Eng.* **41**, 1445–58. (doi:10.1007/s10439-012-0717-y)
45. Formaggia L, Quarteroni A, Vergara C. 2013 On the physical consistency between three-dimensional and one-dimensional models in haemodynamics. *J. Comput. Phys.* **244**, 92–112. (doi:10.1016/j.jcp.2012.08.001)
46. Blanco P, Feijóo R. 2013 A dimensionally-heterogeneous closed-loop model for the cardiovascular system and its applications. *Med. Eng. Phys.* **35**, 652–667. (doi:10.1016/j.medengphy.2012.07.011)
47. Warwick R, Sastry P, Fontaine E, Poullis M. 2009 Carotid artery diameter, plaque morphology, and hematocrit, in addition to percentage stenosis, predict reduced cerebral perfusion pressure during cardiopulmonary bypass: a mathematical model. *J. Extra Corpor. Technol.* **41**, 92–96.
48. Phan DDN, Meyer F, Pech M, Halloul Z. 2015 Length of abdominal aortic aneurysm and incidence of endoleaks type II after endovascular repair. *Wien. Klin. Wochenschr.* **127**, 851–857. (doi:10.1007/s00508-015-0871-y)
49. Hori D, Nomura Y, Yamauchi T, Furuhata H, Matsumoto H, Kimura N, Yuri K, Yamaguchi A. 2019 Perioperative factors associated with aneurysm sac size changes after endovascular aneurysm repair. *Surg. Today* **49**, 130–136. (doi:10.1007/s00595-018-1714-z)
50. Alastruey J, Parker KH, Sherwin SJ. 2012 Arterial pulse wave haemodynamics. In *11th Int. Conf. on Pressure Surges*, ch. 7 (ed. S Anderson), pp. 401–442. Lisbon, Portugal: Virtual PiE Led t/a BHR Group.
51. Figueroa CA, Vignon-Clementel IE, Jansen KE, Hughes TJR, Taylor CA. 2006 A coupled momentum method for modeling blood flow in three-dimensional deformable arteries. *Comput. Methods Appl. Mech. Eng.* **195**, 5685–5706. (doi:10.1016/j.cma.2005.11.011)
52. Moireau P, Xiao N, Astorino M, Figueroa CA, Chapelle D, Taylor CA, Gerbeau J-F. 2012 External tissue support and fluid-structure simulation in blood flows. *Biomech. Model. Mechanobiol.* **11**, 1–18. (doi:10.1007/s10237-011-0289-z)
53. Gaddum N, Alastruey J, Chowienczyk P, Rutten MCM, Segers P, Schaeffter T. 2017 Relative contributions from the ventricle and arterial tree to arterial pressure and its amplification: an experimental study. *Am. J. Physiol. Heart Circ. Physiol.* **313**, H558–H567. (doi:10.1152/ajpheart.00844.2016)
54. Polanczyk A, Podgorski M, Polanczyk M, Piechota-Polanczyk A, Neumayer C, Stefanczyk L. 2018 A novel patient-specific human cardiovascular system phantom (HCSP) for reconstructions of pulsatile blood hemodynamic inside abdominal aortic aneurysm. *IEEE Access* **6**, 61896–61903. (doi:10.1109/ACCESS.2018.2876377)
55. Mariscal-Harana J *et al.* 2021 Estimating central blood pressure from aortic flow: development and assessment of algorithms. *Am. J. Physiol. Heart Circ. Physiol.* **320**, H494–H510. (doi:10.1152/ajpheart.00241.2020)
56. Marsden AL, Vignon-Clementel IE, Chan FP, Feinstein JA, Taylor CA. 2007 Effects of exercise and respiration on hemodynamic efficiency in CFD simulations of the total cavopulmonary connection. *Ann. Biomed. Eng.* **35**, 250–263. (doi:10.1007/s10439-006-9224-3)
57. VanderLaan PA, Reardon CA, Getz GS. 2004 Site specificity of atherosclerosis: site-selective responses to atherosclerotic modulators. *Arterioscler. Thromb. Vasc. Biol.* **24**, 12–22. (doi:10.1161/01.ATV.0000105054.43931.f0)
58. Ailawadi G, Eliason JL, Upchurch GR. 2003 Current concepts in the pathogenesis of abdominal aortic aneurysm. *J. Vasc. Surg.* **38**, 584–588. (doi:10.1016/S0741-5214(03)00324-0)
59. Abdul Khader SM, Shenoy BS, Pai R, Kamath SG, Sharif NM, Rao VRK. 2011 Effect of increased severity in patient specific stenosis of common carotid artery using CFD—a case study. *World J. Model. Simul.* **7**, 113–122.
60. Marshall I, Zhao S, Papathanasopoulou P, Hoskins P, Xu XY. 2004 MRI and CFD studies of pulsatile flow in healthy and stenosed carotid bifurcation models. *J. Biomech.* **37**, 679–687. (doi:10.1016/j.jbiomech.2003.09.032)
61. Matsuura K, Jin WW, Liu H, Matsumiya G. 2018 Computational fluid dynamics study of the end-side and sequential coronary artery bypass anastomoses in a native coronary occlusion model. *Interact. Cardiovasc. Thorac. Surg.* **26**, 583–589. (doi:10.1093/icvts/ivx376)
62. Matsuura K, Jin WW, Liu H, Matsumiya G. 2019 Computational fluid dynamic study of different incision length of coronary artery bypass grafting in a native coronary stenosis model. *J. Thoracic Dis.* **11**, 393–399. (doi:10.21037/jtd.2019.01.35)
63. Willemet M, Alastruey J. 2014 Arterial pressure and flow wave analysis using time-domain 1-D hemodynamics. *Ann. Biomed. Eng.* **43**, 190–206. (doi:10.1007/s10439-014-1087-4)
64. Stergiou YG, Kanaris AG, Mouza AA, Paras SV. 2019 Fluid-structure interaction in abdominal aortic aneurysms: effect of haematocrit. *Fluids* **4**, 11.
65. Salsac AV, Sparks SR, Chomaz JM, Lasheras JC. 2006 Evolution of the wall shear stresses during the progressive enlargement of symmetric abdominal aortic aneurysms. *J. Fluid Mech.* **560**, 19–51. (doi:10.1017/S002211200600036X)
66. Alastruey J *et al.* 2009 Analysing the pattern of pulse waves in arterial networks: a time-domain study. *J. Eng. Math.* **64**, 331–351. (doi:10.1007/s10665-009-9275-1)
67. Bessems D, Rutten M, Van De Vosse F. 2007 A wave propagation model of blood flow in large vessels

using an approximate velocity profile function. *J. Fluid Mech.* **580**, 145–168. (doi:10.1017/S0022112007005344)

68. Valdez-Jasso D, Bia D, Zócalo Y, Armentano RL, Haider MA, Olufsen MS. 2011 Linear and nonlinear viscoelastic modeling of aorta and carotid pressure–area dynamics under *in vivo* and *ex vivo* conditions. *Ann. Biomed. Eng.* **39**, 1438–1456. (doi:10.1007/s10439-010-0236-7)
69. Simakov SS, Gamilov TM, Kopylov FYu, Vasilevskii YuV. 2016 Evaluation of hemodynamic significance of stenosis in multiple involvement of the coronary vessels by mathematical simulation. *Bull. Exp. Biol. Med.* **162**, 111–114. (doi:10.1007/s10517-016-3558-0)
70. Ge X, Liu Y, Tu S, Simakov S, Vassilevski Y, Liang F. 2019 Model-based analysis of the sensitivities and diagnostic implications of FFR and CFR under various pathological conditions. *Int. J. Numer. Methods Biomed. Eng.*, e3257. (doi:10.1002/cnm.3257)
71. Sen S *et al.* 2012 Development and validation of a new adenosine-independent index of stenosis severity from coronary waveintensity analysis: results of the ADVISE (ADenosine Vasodilator Independent Stenosis Evaluation) study. *J. Am. Coll. Cardiol.* **59**, 1392–1402. (doi:10.1016/j.jacc.2011.11.003)
72. Gamilov TM, Kopylov PY, Pryamonosov RA, Simakov SS. 2015 Virtual fractional flow reserve assessment in patient-specific coronary networks by 1D hemodynamic model. *Russian J. Numer. Anal. Math. Model.* **30**, 269–276. (doi:10.1515/rnam-2015-0024)
73. Charlton PH, Mariscal Harana J, Vennin S, Li Y, Chowienczyk P, Alastruey J. 2019 Modeling arterial pulse waves in healthy aging: a database for in silico evaluation of hemodynamics and pulse wave indexes. *Am. J. Physiol. Heart Circ. Physiol.* **317**, H1062–H1085. (doi:10.1152/ajpheart.00218.2019)
74. Chakshu NK, Sazonov I, Nithiarasu P. 2021 Towards enabling a cardiovascular digital twin for human systemic circulation using inverse analysis. *Biomech. Model. Mechanobiol.* **20**, 449–465. (doi:10.1007/s10237-020-01393-6)